Solar Energy Materials & Solar Cells 209 (2020) 110418

Contents lists available at ScienceDirect

Solar Energy Materials and Solar Cells

journal homepage: http://www.elsevier.com/locate/solmat

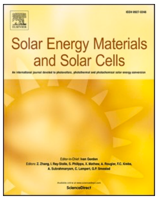

Elucidating the origin of external quantum efficiency losses in cuprous oxide solar cells through defect analysis

Jiantuo Gan [b,1], Robert L.Z. Hoye [a,2], Yulia Ievskaya [a], Lasse Vines [b], Andrew T. Marin [a,3], Judith L. MacManus-Driscoll [a,*], Edouard V. Monakhov [b,**]

[a] Department of Materials Science and Metallurgy, University of Cambridge, 27 Charles Babbage Road, Cambridge, CB3 0FS, UK
[b] University of Oslo, Department of Physics/Center for Materials Science and Nanotechnology, P.O. Box 1048 Blindern, N-0316, Oslo, Norway

ARTICLE INFO

Keywords:
Cuprous oxide solar cells
Atmospheric pressure spatial atomic layer deposition
chemical vapour deposition
Interface and bulk defects
Impedance spectroscopy
Quantum efficiency

ABSTRACT

Heterojunction Cu_2O solar cells are an important class of Earth-abundant photovoltaics that can be synthesized by a variety of techniques, including electrochemical deposition (ECD) and thermal oxidation (TO). The latter gives the most efficient solar cells of up to 8.1% reported in the literature, but is limited by low external quantum efficiencies (EQE) in the long wavelength range (490–600 nm). By contrast, ECD Cu_2O gives higher short wavelength EQEs of up to 90%. We elucidate the cause of this difference by characterizing and comparing ECD and TO films using impedance spectroscopy and fitting with a lumped circuit model to determine the trap density, followed by simulations. The data indicates that TO Cu_2O has a higher density of interface defects, located approximately 0.5 eV above the valence band maximum (N_V), and lower bulk defect density thus explaining the lower short wavelength EQEs and higher long wavelength EQEs. This work shows that a route to further efficiency increases of TO Cu_2O is to reduce the density of interface defect states.

1. Introduction

Heterojunction solar cells with *p*-type Cu_2O (with a direct forbidden bandgap of 2.1 eV) are appealing because they are non-toxic, composed of Earth-abundant elements, and can be synthesized by a variety of techniques [1–6]. These techniques include electrochemical deposition (ECD) and thermal oxidation (TO) [6–13]. A variety of *n*-type buffer layers have been used, including ZnO [7,8], zinc magnesium oxide ($Zn_{1-x}Mg_xO$) [6,9,10], amorphous zinc tin oxide [1],zinc germanium oxide ($Zn_{1-x}Ge_xO$) [13], gallium oxide [14], and aluminum gallium oxide [12].

The theoretical power conversion efficiency of Cu_2O solar cells is expected to reach 18–23% [1,4,6,8,15], but experimental values currently vary between 1–8% [1,6,9,11,13,16]. Losses can arise from non-radiative recombination centers or a limited minority carrier collection length [17,18]. Non-radiative recombination centers include crystallographic defects, impurities or other carrier traps (in the bulk or at the interfaces). These defects can affect the open-circuit voltage (V_{OC}), fill factor (FF) and short circuit current density (J_{SC}) [19]. Interfacial defects can exist in the form of layers or 'islands' of CuO (cupric oxide) from different processing methods [4,6,20,21], from chemical interaction/reaction of the two interfacial materials, or they can originate from the lattice mismatch at the hetero-interface [22,23]. Bulk defects can originate from contaminants in the electrodeposition solution, structural defects (*e.g.*, grain boundaries or stacking faults) or intrinsic defects, such as copper vacancies [24,25]. On the other hand, the minority carrier collection length depends on the mobility and carrier lifetime in Cu_2O [18]. TO films tend to have higher mobilities due to larger grains [26,27], resulting in longer minority carrier collection lengths [18]. As a result, TO Cu_2O has larger long wavelength EQEs than ECD Cu_2O, with longer diffusion length (300–400 nm in the TO samples *vs*. 160 nm in ECD samples [18,28]) [6,14]. However, TO Cu_2O solar cells are limited by a low EQE at short wavelengths (375–490 nm) [6], whereas ECD Cu_2O solar cells have EQEs of 80% or larger in this region

---

* Corresponding author.
** Corresponding author.
E-mail addresses: jld35@cam.ac.uk (J.L. MacManus-Driscoll), edouard.monakhov@fys.uio.no (E.V. Monakhov).
[1] School of Materials Science and Engineering, Xi'an Shiyou University, Xi'an 710065, People's Republic of China (J.G.).
[2] Department of Materials, Imperial College London, Exhibition Road, London SW7 2AZ, UK (R.L.Z.H.).
[3] Intel Corp, UK

https://doi.org/10.1016/j.solmat.2020.110418
Received 28 October 2019; Received in revised form 11 January 2020; Accepted 15 January 2020

[14,18]. Understanding the reason for this difference is important to achieve future efficiency improvements.

To study the differences in EQE, $Cu_2O/Zn_{0.8}Mg_{0.2}O$ heterojunction (HJ) solar cells were made. The Cu_2O was fabricated by both TO and ECD, while the $Zn_{0.8}Mg_{0.2}O$ buffer layer was deposited on top by atmospheric pressure chemical vapor deposition (AP-CVD) using previously reported conditions [6,9]. In AP-CVD, the metal precursor and oxidant gas precursors are introduced through different channels, and react to deposit the oxide under atmospheric pressure, with an order of magnitude higher growth rate than standard ALD, but with similar quality films [2,3]. We have found AP-CVD to be highly advantageous for rapidly depositing pinhole-free, thin (10–200 nm) oxide buffer layers for both ECD and TO Cu_2O solar cells [6,9].

We characterized these devices by impedance spectroscopy and developed an equivalent lumped circuit model to analyze and compare differences in interfacial and bulk traps. In the model, a pair of resistors and capacitors were used in series to simulate the electrical response of active defects located both in the bulk and at the interface, and the differential capacitance $\omega \cdot dC/d\omega$ was used to determine the trap density from frequency sweeps in impedance spectroscopy. By comparing the traps in ECD Cu_2O with TO Cu_2O, we conclude that TO Cu_2O exhibits a higher density of interface traps. Through SCAPS simulations, we confirmed that this correlates with a reduced short wavelength EQE. We determine that further efficiency improvements to TO Cu_2O heterojunctional solar cells could come about by improving the interface with less interface defect recombination.

2. Results and discussion

2.1. *Developing a lumped circuit model of Cu_2O–$Zn_{1\text{-}x}Mg_xO$ solar cells*

A lumped resistor-capacitor (RC) circuit (Fig. 1a) can be established to describe the electrical response of a complete *p-n* junction (including metal-semiconductor junctions) [29,30]. For the $Cu_2O/Zn_{0.8}Mg_{0.2}O$ HJ in the current study, the circuit is comprised of two types of junctions: (1) the *p-n* junction (between $Cu_2O/Zn_{0.8}Mg_{0.2}O$) and (2) two metal-semiconductor junctions, Ag/ITO/Al doped ZnO (AZO)/$Zn_{0.8}Mg_{0.2}O$ and Cu_2O/Au (or Cu_2O/ITO for the anode of ECD Cu_2O). In Fig. 1a, R_{nc} and R_{pc} are the contact resistances for Ag/ITO/(AZO)/$Zn_{0.8}Mg_{0.2}O$ and Cu_2O/Au (or Cu_2O/ITO) junctions, respectively. Dynamic resistance and capacitance associated with surface states at the metal-semiconductor interface are denoted by R_{ns} and C_{ns} for Ag/ITO/(AZO)/$Zn_{0.8}Mg_{0.2}O$, R_{ps} and C_{ps} for Au/Cu_2O (or Cu_2O/ITO). In order to analyze the depletion region of the HJ, the circuit was divided into an infinite number of small segments by geometry and each segment (i.e. the *i*th segment) consists of resistors and capacitors connected in parallel (ΔC_i and ΔR_i) and series (ΔC_{ti} and ΔR_{ti}). In the $Cu_2O/Zn_{0.8}Mg_{0.2}O$ HJ, Cu_2O (*p*-type, $N_A \approx 10^{14}$–10^{15} cm^{-3}) [17] is usually ~2–4 orders of magnitude lower than $Zn_{0.8}Mg_{0.2}O$ (*n*-type, $N_D = \sim 10^{17}$–10^{19} cm^{-3}) [17], forming an abrupt heterojunction, see Fig. 1b. As a result, ΔC_i and ΔR_i in Fig. 1a are geometry related elements and can be expressed by Equations (1a) & (1b) [29], while ΔC_{ti} and ΔR_{ti} are dynamic (or defect) related elements and can be expressed by Equations Eq (1c) and (1d) [31]:

$$\Delta C_i = \frac{\varepsilon}{\Delta x} \tag{1a}$$

$$\frac{1}{\Delta R_i} = \Delta G_i = \frac{\sigma}{\Delta x} \tag{1b}$$

$$\Delta C_{ti} = q^2 N_t(x) \Delta x \tag{1c}$$

$$\frac{1}{\Delta R_{ti}} = \Delta G_{ti} = \frac{\Delta C_{ti}}{\tau_t(x)} \tag{1d}$$

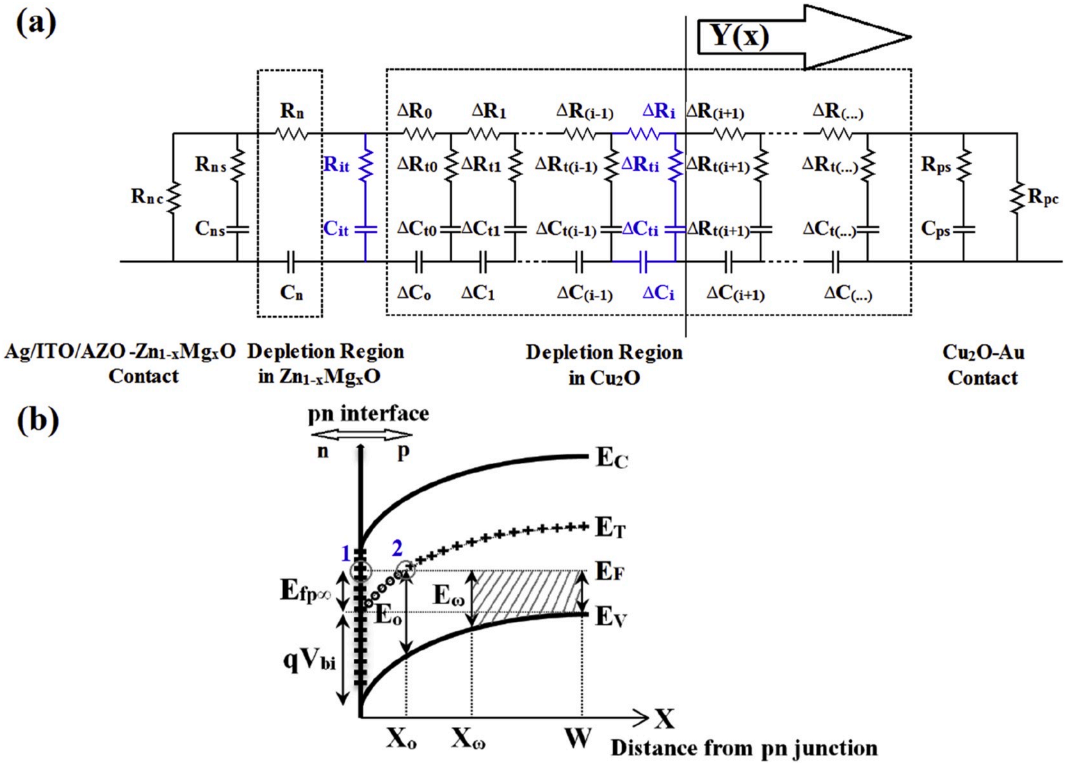

Fig. 1. (a) An equivalent lumped resistor-capacitor (RC) circuit that represents the $Cu_2O/Zn_{0.8}Mg_{0.2}O$ p-n junction, including two metal-semiconductor junctions. ΔR_i and ΔC_i are the geometry related resistance and capacitance, while ΔR_{ti} and ΔC_{ti} are dynamic ones, which are related to the defects in Cu_2O or at interface. (b) Schematic of band diagram for $Zn_{0.8}Mg_{0.2}O/Cu_2O$ abrupt heterojunction. Numbers 1 and 2 in blue are used to denote the cross-section points of Fermi level (E_F) with interface defects and bulk defect level (E_T), respectively. Fig. 1b is reproduced with permission [17]. Copyright 2013, American Institute of Physics. (For interpretation of the references to color in this figure legend, the reader is referred to the Web version of this article.)

In Equations (1a) & (1b), ε and σ are the dielectric constants and conductivity of Cu_2O respectively. Δx is the thickness of the ith segment. In Equation (1c), N_t is denoted as the trap density, q the electron charge and ΔC_{ti} the capacitance associated with a certain trap, which models the capture and emission of carriers from the trap. The conductance of the trap, ΔG_{ti}, can be related to ΔC_{ti} by Equation (1d), where τ_t is the time constant of a trap and the reciprocal of its angular frequency, ω. As a result, elements associated with traps are frequency dependent. The relation between frequency and energy levels can be expressed by Equation (2a) [17]:

$$\omega(E_\omega) = \frac{2\pi}{\tau_t(E_\omega)} = 2\pi(\sigma_i v_{th} N_V) e^{-E_\omega/kT} \tag{2a}$$

$$\omega_o = \omega(E_o) = 2\pi(\sigma_j v_{th} N_V) e^{-E_o/kT} \tag{2b}$$

In Equations (2a) & (2b), σ_j is the capture cross-section of a trap, v_{th} the thermal velocity, N_V the density of states at the Cu_2O valence band, E_ω the corresponding energy position at x_ω (Fig. 1a). $\omega(E_\omega)$ in Equation (2a) has an inverse exponential relationship with E_ω. The angular frequency, ω, can therefore be expressed as the corresponding trap frequency, ω_o, when the energy level, E_ω, is equal to E_o for a bulk defect level at the location x_o (Equation (2b)). In Equations (2a) & (2b), σ_j is the capture cross-section of a trap, v_{th} the thermal velocity, N_V the density of states at the Cu_2O valence band, E_ω the corresponding energy position at x_ω (Fig. 1a). $\omega(E_\omega)$ in Equation (2a) has an inverse exponential relationship with E_ω. The angular frequency, ω, can therefore be expressed as the corresponding trap frequency, ω_o, when the energy level, E_ω, is equal to E_o for a bulk defect level at the location x_o (Equation (2b)).

Before establishing the theoretical model, three approximations were made:

(1) Contact resistances (R_{nc}, R_{pc}) were neglected here even if a small Schottky barrier exists for both types of solar cells, with the one in the ECD Cu_2O sample being more significant (Nyquist plots in Fig. S1). This approximation is valid because, in the model, these two parameters are associated in the circuit in a parallel fashion, which makes it constant in the differential capacitance measurement;

(2) For simplicity, surface states at the metal-semiconductor junctions (R_{ns} and C_{ns} for Ag/ITO/AZO/$Zn_{0.8}Mg_{0.2}O$, R_{ps} and C_{ps} for Au/Cu_2O) were neglected [29]. These parameters are slow reacting in comparison to that from the bulk and interface of the device, reflected by the distance from the hetero-interface. In the measurement, the lowest frequency was $\sim 10^2$ rad/s, making it less possible for detecting the influence of two slow reacting regions;

(3) The dimension-related elements for ZnO, R_n and C_n, were ignored. This is valid because Cu_2O/$Zn_{0.8}Mg_{0.2}O$ is an abrupt heterojunction [17,29].

In the equivalent circuit model (Fig. 1a), the frequency response of traps to carriers affects whether a group of electrical elements should be incorporated in parallel to the previous circuit, i.e., whether ΔR_i and ΔC_i are connected in parallel to ΔR_{ti} and ΔC_{ti}. Therefore, the admittance relation between $Y_{pn}(x + \Delta x)$ and $Y_{pn}(x)$ can be formulated as Equation (3) [32].

$$Y_{pn}(x+\Delta x) = \frac{1}{Z_{pn}(x+\Delta x)} = \frac{1}{\frac{1}{Y_{pn}(x)} + \frac{1}{j\omega\Delta C_{ti}} + \frac{1}{\Delta G_{ti}}} \tag{3}$$

In Equation (3), $Z_{pn}(x + \Delta x)$ is the impedance of the p-n junction. Inserting Equations (1a)-(d) into Equation (3) yields Equation (4a). The calculation details can be found in Fig. S2 of the supporting information (SI):

$$\frac{dY_{pn}}{dx} = -\frac{{Y_{pn}}^2(x)}{j\omega\varepsilon + \sigma} + \frac{j\omega q^2 N_t}{1 + j\omega\tau_t} \tag{4a}$$

By inserting Equations (S3)-(S7) into Equation (4a) from Fig. S3:

$$-\frac{\omega}{\lambda}\frac{dY_{pn}}{d\omega} = -\frac{{Y_{pn}}^2(x)}{j\omega\varepsilon + \sigma} + \frac{j\omega q^2 N_t}{1 + j\omega\tau_t} \tag{4b}$$

where λ is an attenuation factor ($\lambda = -kTL_o/\Delta E_\omega$). The admittance consists of real and imaginary components, namely, $Y_{pn} = G_{pn} + jB_{pn}$ and thus can be projected for the two components for the p-n junction.

$$\frac{dB_{pn}}{d\omega} = \frac{\lambda}{\omega}\left(\frac{2G_{pn}B_{pn}\sigma - \omega\varepsilon\left({G_{pn}}^2 - {B_{pn}}^2\right)}{\sigma^2 + \omega^2\varepsilon^2} - \frac{\omega q^2 N_t}{1 + \omega^2{\tau_t}^2}\right) \tag{5a}$$

$$\frac{dG_{pn}}{d\omega} = \frac{\lambda}{\omega}\left(\frac{\sigma\left({G_{pn}}^2 - {B_{pn}}^2\right) + 2G_{pn}B_{pn}\omega\varepsilon}{\sigma^2 + \omega^2\varepsilon^2} - \frac{\omega q^2 N_t\tau_t}{1 + \omega^2{\tau_t}^2}\right) \tag{5b}$$

Further, replacing B_{pn} with ωC_{pn} in Equation (5a), and by rearranging Equation (5a) so that $N_t(C)$ is the subject the trap density, $N_t(C)$, can be obtained. At the same time, the subscript p-n for G, B and C are removed for convenience and Equations (6) are obtained:

$$N_t(C) = \frac{1 + \omega^2{\tau_t}^2}{\omega q^2}\left(\frac{2G\omega C\sigma - \omega\varepsilon\left(G^2 - \omega^2 C^2\right)}{\sigma^2 + \omega^2\varepsilon^2} - \frac{\omega\Delta E_\omega}{kTL_o}\left(\omega\frac{dC}{d\omega} + C\right)\right) \tag{6a}$$

$$N_t(G) = \frac{1 + \omega^2{\tau_t}^2}{\omega^2 q^2 \tau_t}\left(\frac{\sigma\left(G^2 - \omega^2 C^2\right) + 2GC\omega^2\varepsilon}{\sigma^2 + \omega^2\varepsilon^2} - \frac{\omega\Delta E_\omega}{kTL_o}\frac{dG}{d\omega}\right) \tag{6b}$$

$N_t(C)$ is related to the differential capacitance, $\omega \cdot dC/d\omega$, by the second term in Equation (6a). $N_t(G)$ can be related to the differential conductance G in Equation (6b), but further discussion is beyond the scope of this paper.

In Fig. 1b, the Fermi level (E_F) intersects with both interface defects and the bulk trap level (E_T), numbered 1 and 2 respectively. Both types of defects can affect the results of admittance spectroscopy. In order to differentiate interface defects from bulk defects, admittance measurements should be performed at different biases to determine how the differential capacitance, $\omega \cdot dC/d\omega$, is affected [33]. In Fig. 1b, the bulk defect level (E_T) is in general energetically discrete and the energy difference (ΔE_o) is bias independent. Conversely, the interface defects are continuous and the energy difference (E_{fpi}) is bias dependent [33], which is defined as:

$$E_{fpi} = E_{fp\infty} + q(V_{bi} - V) \tag{7}$$

Consequently, the peak of $\omega \cdot dC/d\omega$ from admittance measurements will shift under different biases for interface defect states. Equation (6a) describes N_t for bulk defects. In order to calculate the trap density for interface defects, Equation (8) from the literature can alternatively be used as a simple approach [33]:

$$N_{it} = -\frac{2}{q^2}\omega\frac{dC}{d\omega} \tag{8}$$

In Equation (8), the differential capacitance, $\omega \cdot dC/d\omega$, is also used for trap density calculations in a similar way to Equation (6a).

To determine the trap density for bulk defects, N_t, of the heterojunction, Equation (6a) can be solved numerically. In the current study, the Ordinary Differential Equation (ODE) function in MATLAB® was used. Before solving Equation (6a), some important parameters needed to be estimated or calculated from the literature, i.e., Debye length, thermal velocity, trap capture cross-section, thickness distribution of the depletion region at each side of the HJ. Initial conditions, such as N_t and trap energy level, are also needed to numerically solve the differential equations. Here, the first term in Equation (6a) according to the above mentioned numerical analysis does not obviously change the capacitance of the p-n junction and thus can be removed from the equation, at the same time C in the second term is removed for the same reason, resulting in a reduced form as Equation (9) [30,33]:

$$N_t = -\frac{\Delta E_\omega}{kTL_o}\frac{1+\omega^2{\tau_t}^2}{q^2}\omega\frac{dC}{d\omega} \tag{9}$$

Below is an example of the result from the numerical analysis. In the bias dependent measurements (Fig. 2a–b), the peaks of the differential capacitance $\omega\cdot dC/d\omega$ are plotted against the angular frequency under different applied biases (from −0.5 to 0.5 V). For bulk traps (Fig. 2a), the peaks at each bias are plotted in such a way that they align at one frequency ($\omega = 1.7\times10^4$ rad s^{-1}) depending on the bulk trap energy level above E_V. The intensity of peaks increases from reverse to forward bias. The exception is for 0.5 V forward bias, where the $\omega\cdot dC/d\omega$ peak is absent because the probing energy, E_ω, would otherwise be smaller than E_{VF} at the highest frequency (Fig. 1b), which is physically impossible. The increase in peak intensity from reverse to forward bias indicates a higher bulk trap density at larger bias as a result of the trap density being proportional to $\omega\cdot dC/d\omega$ (Equation (9)). This is reasonable because the capture cross-section between the trap level and Fermi level is larger with the lower band bending under forward bias (Fig. 1b). By contrast, for interface defects (Fig. 2b), the peaks shift evenly from low to high frequencies for applied biases between −0.1 V and 0.1 V. This peak shift is due to ΔE_ω is being highly influenced by the external applied voltage for interface defects, as reflected by the voltage dependence of E_{fpi} (Eq. (7)). Whereas for the bulk defects, ΔE_ω remains constant because the applied bias does not change the bulk trap energy level.

In Fig. S1c, the differential capacitance $\omega\cdot dC/d\omega$ shifts its peak position in angular frequency, ω, (from 1.2×10^5 to 1.7×10^4 rad s^{-1}) with increasing temperature (from 22 °C to 72 °C). The main reason for the shifts can be explained by Equation (2b), where the angular frequency of a trap (ω_o) is dependent on the thermal energy, kT. In order to extract ΔE_o (bulk trap energy level above N_V) from Fig. S1c, the results of $\ln(\omega_o)$ and $(kT)^{-1}$ are obtained and summarized in Table 1. Rewriting Equation (2b), Equation (10) can be obtained:

$$\ln(\omega_o) = -\frac{\Delta E_o}{kT} + \ln\left(2\pi\sigma_j v_{th} N_V\right) \tag{10}$$

As a result, the Arrhenius plot can be made based on the temperature-dependent measurements (Fig. 2d), with ΔE_o as the slope of the $\ln(\omega_o)$ and $(kT)^{-1}$ plot.

In order to determine ΔE_o, Equation (6a) can again be solved numerically with an initial value of trap energy, 0.45 eV from the valence band, as obtained from the literature [17], so that under different temperatures (22–72 °C), the differential capacitance can be plotted with frequency in Fig. 2c. Further, values of ln (ω_o) and $-1/kT$ are extracted from Fig. 2c, and are listed in Table 1 and displayed in Fig. 2d, so that ΔE_o can be extracted. The extracted ΔE_o is ~0.43 ± 0.01 eV and agrees well with the initial value. This actually further indicates the validity of Equation (6a) for trap density determination. The

Table 1
Results of the peak maximum ($\ln\omega_o$ and kT^{-1}) at each temperature for bulk traps.

	T (K)					
	297	307	317	327	337	347
kT^{-1} (eV^{-1})	39.4	38.1	36.9	35.7	34.7	33.6
$\ln\omega_o$ ($rad\cdot s^{-1}$)	11.6	12.3	12.9	13.5	14.0	14.5
ω_o ($rad\cdot s^{-1}$)	1.2×10^5	2.4×10^5	4.2×10^5	7.5×10^5	1.3×10^6	2.1×10^6

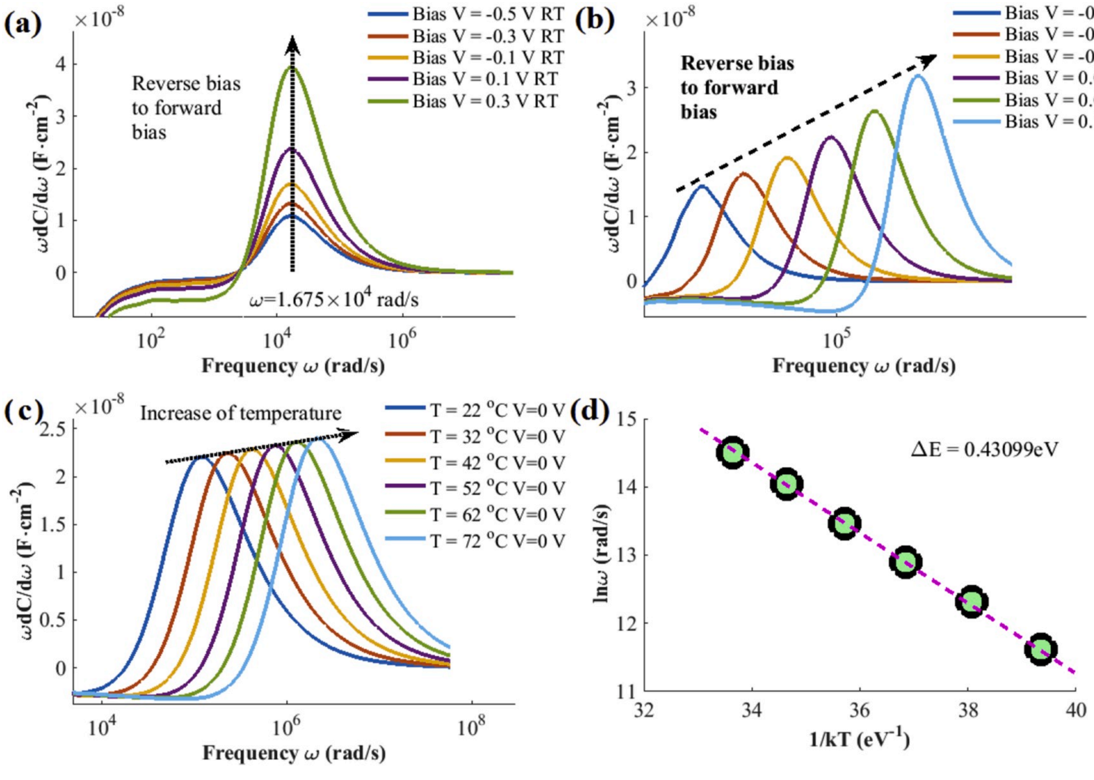

Fig. 2. (a) Differential capacitance $\omega\cdot dC/d\omega$ with respect to angular frequency ω under different bias conditions from −0.5 V to 0.5 V from numerical results in Eq. (6) to analyze bulk defects. The bias at 0.5 V did not give any result in the plot, the reason of the plot measured at forward 0.5 V is missing is because the probing energy E_ω at the highest frequency is smaller than E_{VF}). (b) Differential capacitance $\omega\frac{dC}{d\omega}\omega\cdot dC/d\omega$ with respect to angular frequency ω under different bias conditions from −0.1 V to 0.1 V from simulation to analyze interface defects. (c) Differential capacitance $\omega\cdot dC/d\omega$ with respect to angular frequency ω under different temperatures from 22 °C to 72 °C from simulation to analyze bulk defects (d) Extraction of the trap energy ΔE_o from shifts of $\omega\frac{dC}{d\omega}\omega\cdot dC/d\omega$ peaks with temperatures from Fig. 2c.

difference of 0.02 eV between the value obtained by fitting the measurements and the literature value can be considered as numerical errors in the simulation (given that kT is 0.025 eV). The measurements at different temperatures is also complicated by the heating of the Cu_2O and possible formation of CuO at the heterojunction at above 50 °C during the growth of the $Zn_{0.8}Mg_{0.2}O$ layer [10]. As a result, we will focus on the bias-dependent measurements in this work. We have therefore developed the necessary analytical techniques and methodology for measuring the defect states present in our $Cu_2O/Zn_{1-x}Mg_xO$ HJs.

2.2. *Performance of $Cu_2O/Zn_{0.8}Mg_{0.2}O$ solar cells*

We made test on devices from both TO and ECD Cu_2O. The *J–V* curves measured under 1 sun AM 1.5G illumination is shown in Fig. 3a. From these, the performance parameters were calculated and shown in Table 2. We have previously found the optimal deposition temperature for $Zn_{0.8}Mg_{0.2}O$ is with thermally oxidized Cu_2O underlayer being held at 150 °C [6], which we used here. For comparison, we also deposited $Zn_{0.8}Mg_{0.2}O$ with ECD Cu_2O (ECD05) at 150 °C. On the other hand, we have previously found the device performance to be improved at lower deposition temperatures (80 °C) [9]. Hence, we also used this lower deposition temperature for the fabrication of a further ECD sample, ECD03. Irrespective of the Cu_2O deposition method (TO or ECD), we obtained PCEs of approximately 1% in the Cu_2O devices. But the causes are quite different. For the ECD03 Cu_2O sample, the FF is higher (53%) but it has a lower J_{SC} (4.4 mA·cm^{-2}) in comparison with those of the TO sample (35% and 8.3 mA·cm^{-2}). Typically, the difference in the contributions to the PCEs for the ECD and TO Cu_2O samples suggests that the recombination mechanisms are not the same, as discussed further below.

Despite the comparable efficiencies, the TO and ECD Cu_2O devices had different EQEs (Fig. 3b). Whereas the TO Cu_2O had a higher EQE in the long wavelength range (490–600 nm), its EQE dips by approximately 20% at wavelengths between 400 nm and 490 nm, consistent with previous reports [6,12]. By contrast, the EQE of the ECD Cu_2O reached ~90% in the short wavelength range, even for ECD05 (Fig. 3b). In order to clarify the differences in the EQE results, the drift-diffusion model by Musselman et al. [18] was used to model the charge transport length in both types of devices. The results showed than the diffusion length of minority carriers in the TO sample is 310 nm, three times of that of the ECD sample. Consequently, this leads to a large EQE at long wavelengths. Our results agree well with the diffusion lengths obtained from earlier studies. However, the efficiency of the TO sample is still limited by a poor hetero-interface [6], even though it has a longer drift length of minority charge carriers (2790 nm) than the ECD sample (110 nm drift length) [18]. Musselman et al. [18] was successful in using the drift-diffusion model to determine the charge transport diffusion for TO and ECD samples. However, the underlying mechanisms and the fundamental reasons for the difference between the two samples were not explored. On the other hand, Marin et al. [33] introduced admittance spectroscopy as a means to determine the trap density of hetero-interfaces in Cu_2O based PV solar cells. But they did not differentiate between the two major recombination pathways. In particular, the reason for the low short wavelength EQE in thermally oxidized Cu_2O device was not determined. To answer these questions, in this work, we established a lumped circuit model to differentiate the effects of interface and bulk detects on efficiency losses in these two samples.

Table 2
Parameters extracted from the *J–V* measurements for the two types of $Cu_2O/Zn_{0.8}Mg_{0.2}O$ heterojunction solar cells.

Samples	$Zn_xMg_{1-x}O$ deposition temperature (°C)	V_{OC} [V]	J_{SC} [mA·cm^{-2}]	FF [%]	η [%]
ECD03 Cu_2O	80	0.43	4.4	53	1.02
ECD05 Cu_2O	150	0.33	5.0	34	0.55
TO Cu_2O	150	0.34	8.3	35	0.99

Apart from the efficiency losses in Cu_2O solar cells due to these defects, other factors could also play a strong role in determining their V_{OC}s and associated efficiencies. For example, Cendula et al. found that a theoretical photovoltage (1.7 V, approaching the E_g (2.1 V) in Cu_2O) is expected to be achieved by adjusting the electron affinity of the charge transport layers [1]. Indeed, on a laboratory scale, Minami et al. have achieved a high power conversion efficiency (PCE, 8.1%) in Cu_2O solar cells using a heterostructure of MgF_2/AZO/$Zn_{1-x}Ge_xO/Cu_2O$:Na [13]. Interestingly, they showed that the PCEs (0–8.1%) of the Cu_2O solar cells are critically dependent on the oxygen gas pressure (2–8 Pa) during synthesis of $Zn_{1-x}Ge_xO$, in addition to the Ge content and the thickness of the $Zn_{1-x}Ge_xO$ layer. The improvement in PCE for their Cu_2O devices are explained as reduction in the conduction band discontinuity between the charge transport layer $Zn_{1-x}Ge_xO$ and the photo-absorber Cu_2O:Na by tuning the electron affinity of $Zn_{1-x}Ge_xO$. This leads to a large V_{OC} (approximately 1.2 V) in their Cu_2O solar cells. This is consistent with the results from the theoretical study by Cendula et al. using a drift-diffusion semiconductor model [34]. Indeed, a large conduction band discontinuity would accentuated the effects of the interface defects.

2.3. *Defect analysis of $Cu_2O/Zn_{0.8}Mg_{0.2}O$ heterojunctions*

A lumped circuit model with impedance spectroscopy was used to analyze TO and ECD samples (ECD03 and ECD05, respectively, with more details on impedance analysis of ECD05 shown in Fig. S4). In the

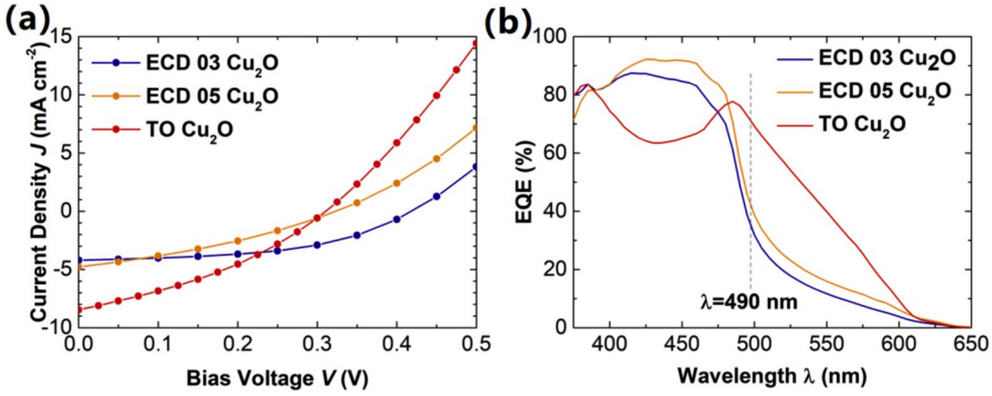

Fig. 3. (a) Plots of current density versus bias voltage (*J–V*) for both types of samples under illumination of AM 1.5G radiation. (b) Plots of external quantum efficiency (EQE) for both types of samples.

Nyquist plots for the two types of samples, the imaginary component of the impedance (–Z”) is plotted against the real component (Z) under an applied D.C. bias of −0.5 V–0.5 V. The Nyquist plots are depressed semicircles at each D.C. bias, in which the center is below the Z’ axis (i.e., –Z” < Z’ at the maximum for –Z”), which indicates that a defect-related impedance component should be added to the model [33]. A separate small semicircle was also present in the low impedance region for both types of samples. But for the TO Cu_2O, the smaller semicircle merged into the larger semicircle (Fig. S1b’), indicating that Schottky contacts have less of an influence than for ECD03 (Fig. S1a’).

Analyzing the differential capacitance plots gives an indication of the defect states present. For ECD03 (Fig. 4a), there is only one differential capacitance peak at each D.C. bias and the peak intensity showed a slight increase with applied biases from −0.5 V to 0.3 V, but then reduced to a lower intensity at a bias of 0.5 V. At the same time, the peak position shifted from 3.7×10^4 rad s^{-1} to 2.7×10^5 rad s^{-1} with increasing D.C. bias. In a first approximation, the bias dependent differential capacitance for the ECD sample may seem to have followed the trend of interface defects. However, the magnitude of the bias dependent peak indicated in Fig. 2b for interface defects shows a strong shift in frequency within a voltage range of −0.1 V–0.1 V. Hence, the experimental peak shift in the ECD sample does not seem to match the characteristics of interface defects. Because a small shift in these peaks means little variation of trap energy, formulated by Equation (2a), where frequency is related to the energy, contradicting the nature of continuous energy distribution of the interface traps (0.4–0.8 eV above valence band) [17]. Using this equation, however, the peak shift in the ECD sample indicated a bias dependent trap energy (E_o) of ~0.44–0.48 eV, with trap energy of 0.46 eV for zero bias. If bulk defects are allowed to vary within a certain range, e.g., due to its density distribution with energy, or formation of bulk defects in band, with external bias, then it is reasonable to attribute these peaks to bulk defects. Indeed, a defect band was observed in the as-deposited Cu_2O film and was claimed as the main reason for difference in optical absorption [35]. Therefore, it is surmised that the peak shift in the ECD sample is caused by a band defect and the bulk defects are located 0.46 ± 0.02 eV above E_V. This agrees with early observation of trap density at 0.475 eV for Cu_2O from deep level transient spectroscopy (DLTS) [36]. Further, assignment of the peaks to bulk defects hinges on the observation of long wavelength EQE loss in the ECD sample.

From the differential capacitance plots for the thermally oxidized Cu_2O device (Fig. 4b), the angular frequency (ω_o, aligned at 1.2×10^4 rad s^{-1}) was unchanged with applied bias. In contrast, the peak intensity increased with applied biases of −0.5 V–0.3 V, before dropping at 0.5 V. Again, according to the bias dependent feature of the differential peaks, the alignment of peaks for frequency can thus be tentatively assigned to bulk defects. However, the peak intensity in the thermally oxidized sample does not increase by the same magnitude as it does from the bulk defects (in Fig. 2a), thus not reflecting the effect of band bending in defect activity with external biases. In fact, both the J–V and EQE measurements (Fig. 3) suggest that interface defects played important roles for the thermally oxidized Cu_2O device. If so, one possibility for the absence of peak shifts with external bias in this device is that a large density of interface defects can pin the Fermi level and prevent the shift of the differential capacitance peaks under applied bias [33]. At interfaces, traps can be generated as a result of, e.g., dangling bonds or strain induced formation of CuO [21]. Fermi level pinning occurs when a particular vacancy or interstitial accumulates at the surface, resulting in the localization of these defects in energy [33]. The pinning of the Fermi level may result in lower band-bending at the heterojunction, resulting in a smaller built-in voltage, which may contribute to the lower V_{OC} of the thermally oxidized Cu_2O device (Table 2), and further the observed dip in EQEs at the short wavelength. We note that the thermally oxidized sample, which a V_{OC} of 0.336 V is much lower than that (0.43 V) of the ECD sample. At this moment, therefore, the peaks at $\omega_o \sim 10^4$ rad s^{-1} for the thermally oxidized Cu_2O is assigned to pinned interface defects with $E_{fpi} \approx 0.5$ eV above E_V [17]. Further information is discussed in Sec. 2.4.

We also note that, in the thermally oxidized sample, there is a differential capacitance shoulder located at $\omega_o \sim 10^6$ rad s^{-1} (Fig. 4b) with lower intensity, and its intensity becomes larger at forward biases. Using Equation (2a), the corresponding energy level of the shoulders is ~0.27 eV above the N_V. This shoulder is most probably related to the inhomogeneity at the heterojunction, rather than a perturbation by a Schottky barrier [17,33]. The inhomogeneity can cause varying profiles of energy level for defects. The appearance of such a shoulder is a characteristic feature of interface defects. In addition, as stated in Sec.2.1, items (1) and (2) resistances at the metal/semiconductor contact are ignored for simplicity and thus in the simulation results, Fig. 2b&c, there is no trace of such small peaks. In addition, surface defects will affect both the simulation and experimental results at low frequencies because they are further away from the hetero-interface.

The trap density, calculated from Equation (8) (interface defects) and 9 (bulk defects) with our measurements, is shown in Fig. S5. The thermally oxidized Cu_2O has interface defects with a peak in trap density at ~0.5 eV above E_V (Fig. S5a). At the same time, the interface defect shows a variation in energy level to 0.27 eV due to inhomogeneity in the Cu_2O films. On the other hand, the ECD Cu_2O has a band of bulk defects located 0.46 ± 0.02 eV above E_V (Fig. S5b). The distributed bulk defects in the ECD Cu_2O may arise from the higher density of grain boundaries than in the thermally oxidized Cu_2O, which can act as bulk recombination centers [6,9,18]. The trap density in the ECD Cu_2O is also an order of magnitude higher than the interface trap density in the thermally oxidized sample, which could be another reason why the ECD Cu_2O samples have lower long wavelength EQEs (Fig. 3b). For sample ECD05, the differential capacitance peaks align at 6.1×10^4 rad/s for bias voltages varying from −0.5 V to 0.5 V (Fig. S4c). This fits well with

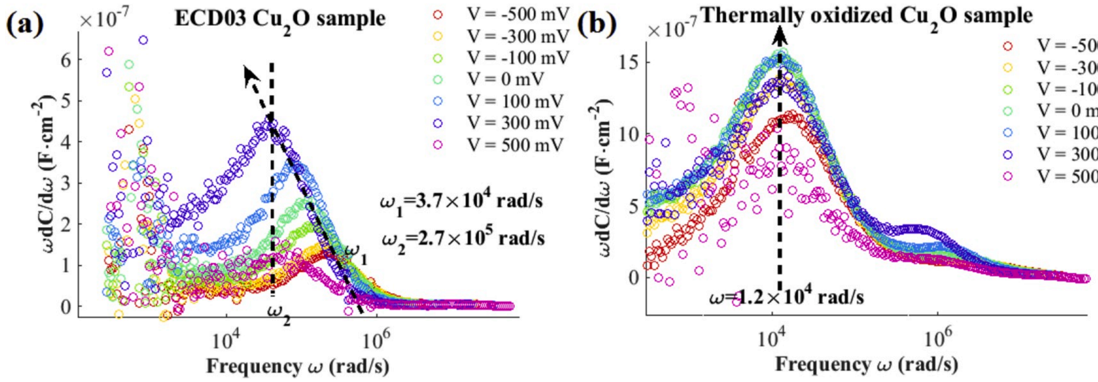

Fig. 4. Differential capacitance $\omega \cdot dC/d\omega$ plots against angular frequency ω (a) ECD Cu_2O with $Zn_{0.8}Mg_{0.2}O$ deposited at 80 °C (ECD03) and (b) thermally oxidized Cu_2O, under different bias conditions at room temperature.

the simulated results, see Fig. 2a, in terms of the alignment of peaks with external biases. Thus, this indicates that the defects are located at a fixed energy level, rather than an energy band for the ECD03 sample. On the other hand, the intensity of these peaks does not change with bias, indicating a uniform trap density. As a result, in comparison with the ECD03 sample, the ECD05 sample shows bulk defects with single energy level at 0.31 eV above N_V.

2.4. Simulations on the influence of interface recombination velocity on EQE

We performed simulations on the $Cu_2O/Zn_{0.8}Mg_{0.2}O$/AZO stack using SCAPS [37]. Using these simulations, we were able to determine the correlation between the defect states we measured and the EQE. For thermally oxidized Cu_2O, we modeled the defects as interface states with a Gaussian distribution centered 0.5 eV above E_V. We compared the EQEs at different trap densities (N_t). When there are no interfacial traps, the EQE is 100% for wavelengths below 490 nm (Fig. 5a). When the trap density increases to 2×10^{12} eV^{-1} cm^{-2} (the same as the N_t measured for ECD Cu_2O), the EQE decreases in the short wavelength range. But with the trap density measured for thermally oxidized Cu_2O (2×10^{13} eV^{-1} cm^{-2}), the simulated EQE was 0%. Simulated EQEs are 0% for trap densities higher than 5.24×10^{12} eV^{-1} cm^{-2}.

We modeled ECD Cu_2O as having a Gaussian distribution of bulk defects centered 0.46 eV above E_V and no interface defects. In this case, the long wavelength EQEs are lower than those for thermally oxidized Cu_2O (Fig. 5), and the short wavelength EQEs are 100% for wavelengths below 490 nm. The trend in long wavelength EQEs is in agreement with our measurements (Fig. 3b). We took the series resistance (20 Ω cm^2) and shunt resistance (300 Ω cm^2) of the device into account in our simulations, but our short wavelength EQEs for ECD Cu_2O may not reach 100% due to losses in the $Zn_{0.8}Mg_{0.2}O$ layer [38], which we did not take to account for simplicity. We also considered the case where the 2×10^{12} eV^{-1} cm^{-2} density of bulk defect states in ECD Cu_2O also occurred at the interface. This again resulted in a decrease in the short wavelength EQEs (Fig. 5b). Our simulations are therefore consistent with our defect analysis that indicates that the lower short wavelength EQEs for thermally oxidized Cu_2O are a result of interfacial defect states.

In order to achieve higher efficiencies in Cu_2O solar cells in the future, interface phenomena (e.g., interface defect recombination and conduction band offset at the heterointerface) between the Cu_2O photoactive layer and the different types of charge transport layer should be further studied. In particular, a higher PCE with a larger V_{OC} (over 1 V) is anticipated in Cu_2O solar cells, where charge carriers can easily cross the heterointerface without being annihilated.

3. Conclusion

We have analyzed defects in Cu_2O made by thermal oxidation (TO) and electrochemical deposition (ECD) by developing a lumped circuit model in impedance spectroscopy measurements. These show that TO Cu_2O predominantly has interfacial defect states centered 0.5 eV above E_V, whereas ECD Cu_2O predominantly has bulk states centered between 0.46 ± 0.02 eV above E_V. Through SCAPS simulations, we found that Cu_2O with predominantly interfacial rather than bulk defect states has higher long wavelength EQEs but lower short wavelength EQEs. This strongly agrees with our EQE measurements of TO and ECD Cu_2O heterojunction solar cells. This work indicates that the route to further improvements in Cu_2O solar cells is by defect control with interface engineering of the TO Cu_2O devices.

4. Experimental section

Cu_2O synthesis: For thermally oxidized cuprous oxide, Cu_2O substrates were obtained by a 2 h oxidation of 0.25 mm thick copper foil, finished by quenching of the substrates, as described in Ref. [6] The oxygen partial pressure was monitored throughout the heat treatment keep the substrates in the phase region where cuprous oxide is thermodynamically stable [24]. Cupric oxide (CuO) formed on the substrate surface during quenching was removed by etching. Substrates were then masked on one side with insulating black paint, defining the solar cell area to be approximately 0.1 cm^2.

Electrochemically deposited (ECD) Cu_2O solar cells were prepared on ITO/glass using a previously reported method [9]. ITO/glass substrates were cleaned by scrubbing with 10 vol% HCl, followed by ultrasonically cleaning for 15 min in water, toluene and isopropanol. Cu_2O was deposited at 40 °C from a solution of 0.2 $mol \cdot L^{-1}$ Cu^{2+} (from $CuSO_4 \cdot 5H_2O$), 1.5 $mol \cdot L^{-1}$ lactic acid and ~ 2 $mol \cdot L^{-1}$ OH^- (from NaOH) to keep the pH at 12.65. The current density was kept constant at -1.5 $mA \cdot cm^{-2}$.

AP-CVD buffer layer deposition: $Zn_{0.8}Mg_{0.2}O$ was deposited on top of the Cu_2O by atmospheric pressure chemical vapor deposition (AP-CVD) [2]. Diethylzinc and bis (ethylcyclopentadienyl) magnesium were used as the Zn and Mg precursors respectively, and deionized water was used as the oxidant source. Nitrogen gas was used to bubble through the precursors at 6 $mL \cdot min^{-1}$ (Zn precursor), 200 $mL \cdot min^{-1}$ (Mg precursor) and 100 $mL \cdot min^{-1}$ (water). The metal precursors were diluted with nitrogen gas flowing at 100 $mL \cdot min^{-1}$, and the oxidant diluted with nitrogen gas flowing at 200 $mL \cdot min^{-1}$. These were fed to a gas manifold, along with nitrogen gas flowing at 500 $mL \cdot min^{-1}$, to create separate channels of metal precursor and oxidant separated by channels of inert

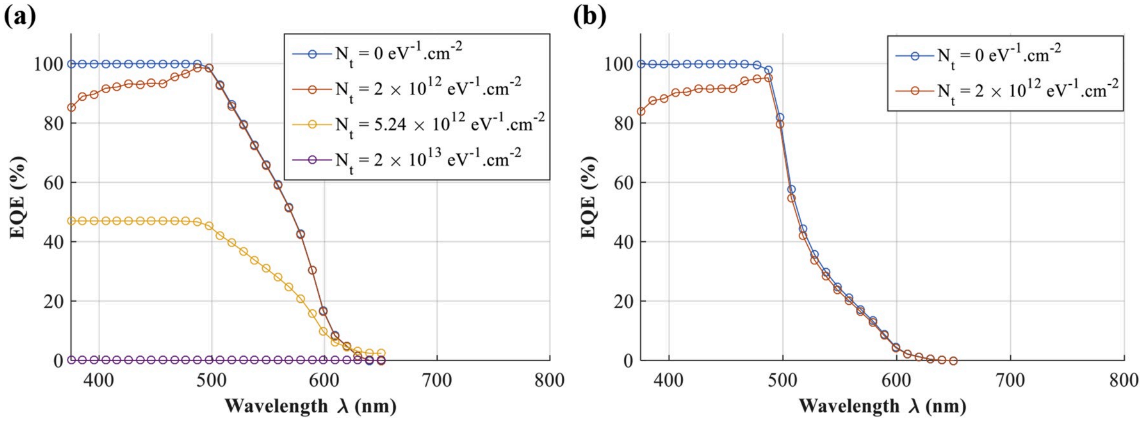

Fig. 5. External quantum efficiency (EQE) of (a) thermally oxidized and (b) ECD Cu_2O devices calculated using SCAPS numerical simulation for different trap densities. The thermally oxidized Cu_2O was modeled with only interfacial recombination, with the defects having a Gaussian distribution located 0.5 eV above E_V. The ECD Cu_2O was modeled with a Gaussian distribution of bulk defects located 0.46 eV above E_V. The capture cross-section was taken as 4.5×10^{-12} cm^2, based on previous measurements [17].

nitrogen gas. 600 oscillations of the substrate beneath the gas manifold was used, giving films of approximately 60 nm in thickness.

Characterization: An Agilent 4294 Precision Impedance Analyzer was used to characterize the impedance spectra against the normal frequency in Hz. The measurement was performed at a certain applied bias voltage with AC signal (amplitude of 20 mV, sweeping from 40 Hz to 10 MHz). The temperature was controlled by using a hotplate and was monitored by a thermocouple. The samples were stored in the darkness for the same period of time (overnight) prior to the experiments in order to empty the traps that became occupied upon light soaking.

Solar simulations were performed under AM 1.5G radiation using an Oriel 92250A solar simulator according to previous reports [6,9]. External quantum efficiency measurements were performed using a 100 W tungsten halogen lamp source and monochromator, according to previous reports [6].

Declaration of competing interest

The authors declare no competing financial interest.

CRediT authorship contribution statement

Jiantuo Gan: Writing - original draft, Writing - review & editing. **Robert L.Z. Hoye:** Writing - original draft, Writing - review & editing. **Yulia Ievskaya:** Writing - original draft, Writing - review & editing. **Lasse Vines:** Writing - original draft, Writing - review & editing. **Andrew T. Marin:** Writing - original draft, Writing - review & editing. **Judith L. MacManus-Driscoll:** Writing - original draft, Supervision, Writing - review & editing. **Edouard V. Monakhov:** Writing - original draft, Supervision, Writing - review & editing.

Acknowledgements

The work is dedicated to Professor Bengt Gunnar Svensson, who was supervisor of J.G. during his Ph.D. thesis study and unfortunately passed away due to heart attack in June 2018 before the manuscript was submitted. This work was conducted under the research project ***Development of a Hetero-Junction Oxide-Based Solar Cell Device (HeteroSolar)***, financially supported by the Research Council of Norway (research project ES483391 with number: 1) through the RENERGI program. The authors also acknowledge the support of the Cambridge Overseas and Commonwealth Trust, the Rutherford Foundation of New Zealand, and the ERC Advanced Investigator Grant, Novox, ERC-2009-adG247276.

Appendix A. Supplementary data

Supplementary data to this article can be found online at https://doi.org/10.1016/j.solmat.2020.110418.

References

[1] Y.S. Lee, J. Heo, S.C. Siah, J.P. Mailoa, R.E. Brandt, S.B. Kim, R.G. Gordon, T. Buonassisi, Energy Environ. Sci. 6 (2013) 2112–2118.
[2] R.L.Z. Hoye, D. Muñoz-Rojas, K.P. Musselman, Y. Vaynzof, J.L. MacManus-Driscoll, ACS Appl. Mater. Interfaces 7 (2015) 10684–10694.
[3] R.L.Z. Hoye, D. Muñoz-Rojas, S.F. Nelson, A. Illiberi, P. Poodt, F. Roozeboom, J. L. MacManus-Driscoll, APL Mater. 3 (2015), 040701.
[4] S.S. Wilson, J.P. Bosco, Y. Tolstova, D.O. Scanlon, G.W. Watson, H.A. Atwater, Energy Environ. Sci. 7 (2014) 3606–3610.
[5] S. Rühle, A.Y. Anderson, H.-N. Barad, B. Kupfer, Y. Bouhadana, E. Rosh-Hodesh, A. Zaban, J. Phys. Chem. Lett. 3 (2012) 3755–3764.
[6] Y. Ievskaya, R.L.Z. Hoye, A. Sadhanala, K.P. Musselman, J.L. MacManus-Driscoll, Sol. Energy Mater. Sol. Cells 135 (2015) 43–48.
[7] K.P. Musselman, A. Wisnet, D.C. Iza, H.C. Hesse, C. Scheu, J.L. MacManus-Driscoll, L. Schmidt-Mende, Adv. Mater. 22 (2010) E254–E258.
[8] T. Gershon, K.P. Musselman, A. Marin, R.H. Friend, J.L. MacManus-Driscoll, Sol. Energy Mater. Sol. Cells 96 (2012) 148–154.
[9] R.L.Z. Hoye, S. Heffernan, Y. Ievskaya, A. Sadhanala, A.J. Flewitt, R.H. Friend, J. L. MacManus-Driscoll, K.P. Musselman, ACS Appl. Mater. Interfaces 6 (2014) 22192–22198.
[10] R.L.Z. Hoye, R.E. Brandt, Y. Ievskaya, S. Heffernan, K.P. Musselman, T. Buonassisi, J.L. MacManus-Driscoll, APL Mater. 3 (2015), 020901.
[11] T. Minami, Y. Nishi, T. Miyata, Thin Solid Films 549 (2013) 65–69.
[12] T. Minami, Y. Nishi, T. Miyata, Appl. Phys. Express 8 (2015), 022301.
[13] T. Minami, Y. Nishi, T. Miyata, Appl. Phys. Express 9 (2016), 052301.
[14] Y.S. Lee, D. Chua, R.E. Brandt, S.C. Siah, J.V. Li, J.P. Mailoa, S.W. Lee, R. G. Gordon, T. Buonassisi, Adv. Mater. 26 (2014) 4704–4710.
[15] J.J. Loferski, J. Appl. Phys. 27 (1956) 777–784.
[16] A. Mittiga, E. Salza, F. Sarto, M. Tucci, R. Vasanthi, Appl. Phys. Lett. 88 (2006) 163502.
[17] A.T. Marin, K.P. Musselman, J.L. MacManus-Driscoll, J. Appl. Phys. 113 (2013) 144502.
[18] K. Musselman, Y. Ievskaya, J.L. MacManus-Driscoll, Appl. Phys. Lett. 101 (2012) 253503.
[19] A. Polman, H.A. Atwater, Nat. Mater. 11 (2012) 174–177.
[20] S.W. Lee, Y.S. Lee, J. Heo, S.C. Siah, D. Chua, R.E. Brandt, S.B. Kim, J.P. Mailoa, T. Buonassisi, R.G. Gordon, Adv. Energy Mater. 4 (2014) 1301916.
[21] J. Gan, S. Gorantla, H.N. Riise, Ø.S. Fjellvåg, S. Diplas, O.M. Løvvik, B.G. Svensson, E.V. Monakhov, A.E. Gunnæs, Appl. Phys. Lett. 108 (2016) 152110.
[22] B.M. Fariza, J. Sasano, T. Shinagawa, H. Nakano, S. Watase, M. Izaki, J. Electrochem. Soc. 158 (2011) D621–D625.
[23] S.-M. Chou, M.-H. Hon, C. Leu, Y.-H. Lee, J. Electrochem. Soc. 155 (2008) H923–H928.
[24] F. Biccari, University of Rome 2012.
[25] A. Soon, X.-Y. Cui, B. Delley, S.-H. Wei, C. Stampfl, Phys. Rev. B 79 (2009), 035205.
[26] Y.S. Lee, J. Heo, M.T. Winkler, S.C. Siah, S.B. Kim, R.G. Gordon, T. Buonassisi, J. Mater. Chem. A 1 (2013) 15416–15422.
[27] K. Bergum, H.N. Riise, S. Gorantla, P.F. Lindberg, I.J. Jensen, A.E. Gunnæs, A. Galeckas, S. Diplas, B.G. Svensson, E. Monakhov, J. Phys. Condens. Matter 30 (2018), 075702.
[28] Y. Liu, H.K. Turley, J.R. Tumbleston, E.T. Samulski, R. Lopez, Appl. Phys. Lett. 98 (2011) 162105.
[29] P. Viktorovitch, G. Moddel, J. Appl. Phys. 51 (1980) 4847–4854.
[30] J. Kneisel, K. Siemer, I. Luck, D. Bräunig, J. Appl. Phys. 88 (2000) 5474–5481.
[31] S. Johansson, M. Berg, K.-M. Persson, E. Lind, IEEE Trans. Electron Devices 60 (2013) 776–781.
[32] Y. Yuan, L. Wang, B. Yu, B. Shin, J. Ahn, P.C. McIntyre, P.M. Asbeck, M.J. W. Rodwell, Y. Taur, IEEE Electron. Device Lett. 32 (2011) 485–487.
[33] A. Marin, University of Cambridge 2013.
[34] P. Cendula, M.T. Mayer, J. Luo, M.J. Grätzel, Sustain. Energy Fuels 3 (2019) 2633–2641.
[35] J. Gan, A. Galeckas, V. Venkatachalapathy, H.N. Riise, B.G. Svensson, E. V. Monakhov, MRS Online Proc. (2015) 1792.
[36] L. Papadimitriou, Solid State Electron. 36 (1993) 431–434.
[37] M. Burgelman, P. Nollet, S. Degrave, Thin Solid Films 361 (2000) 527–532.
[38] R.L. Hoye, B. Ehrler, M.L. Böhm, D. Muñoz-Rojas, R.M. Altamimi, A.Y. Alyamani, Y. Vaynzof, A. Sadhanala, G. Ercolano, N.C. Greenham, Adv. Energy Mater. 4 (2014) 1301544.